# Dynamic principles of concentration buffering through liquid–liquid phase separation

**Logan de Monchaux-Irons, T.-Y. Dora Tang, Christoph A. Weber, Thomas C. T. Michaels**

**Angaben zur Veröffentlichung / Publication details:**

Monchaux-Irons, Logan de, T.-Y. Dora Tang, Christoph A. Weber, and Thomas C. T. Michaels. 2026. "Dynamic principles of concentration buffering through liquid–liquid phase separation." *Proceedings of the National Academy of Sciences (PNAS)* 123 (31): e2526810123. https://doi.org/10.1073/pnas.2526810123.

PNAS RESEARCH ARTICLE | APPLIED PHYSICAL SCIENCES

# Dynamic principles of concentration buffering through liquid–liquid phase separation

Logan de Monchaux-Irons[a,b], T.-Y. Dora Tang[c], Christoph A. Weber[d], and Thomas C. T. Michaels[a,b,1]

Affiliations are included on p. 9.

Edited by Anthony A. Hyman, Max-Planck-Institut fur molekulare Zellbiologie und Genetik, Dresden, Germany; received September 23, 2025; accepted June 12, 2026

**Living systems must maintain robust biochemical function despite fluctuations that span a wide range of timescales. Biomolecular condensates formed by liquid–liquid phase separation (LLPS) have been shown to buffer concentration fluctuations, but the principles governing their dynamic regulation remain unclear. We address this by probing the response of LLPS to oscillatory perturbations that mimic fluctuations across different timescales, establishing the first systematic frequency-domain analysis of concentration buffering by condensates. We find that condensates act as frequency-selective filters: The perturbed dilute phase behaves as a high-pass filter, while the dense phase attenuates both low- and high-frequency perturbations. We establish quantitative links between LLPS parameters, including interaction strength, droplet size, and interphase exchange rates, and the timescale range over which condensates effectively buffer concentration fluctuations. These findings establish fundamental dynamical limits of concentration buffering by LLPS, with implications for how cells may use LLPS to adapt to fluctuating environments and for the design of synthetic condensates with programmable control properties.**

biomolecular condensates | liquid–liquid phase separation | control theory | concentration buffering | biological physics

## Significance

Cellular function depends on stability under fluctuating conditions that occur across diverse timescales. Biomolecular condensates formed by liquid–liquid phase separation have been shown to buffer concentration fluctuations. However, the dynamic response to fluctuations at different timescales remains unclear. Here, we use control theory, analytic modeling, and simulations to reveal the principles of dynamic concentration buffering. We show that condensates act as frequency-selective filters: they suppress slow fluctuations but may transmit fast ones. We identify key timescales and physical parameters that govern buffering effectiveness. These results establish the fundamental dynamical limits of condensate-mediated buffering and provide a general framework for understanding how cells may exploit phase separation to regulate fluctuations.

Cells must function robustly despite constant fluctuations in their molecular environment. Gene expression noise, metabolic variability, and changing external conditions generate protein concentration perturbations across a wide range of timescales (1, 2), necessitating mechanisms to control the cellular environment (3, 4). One suggested control mechanism are biomolecular condensates formed by liquid–liquid phase separation (LLPS) of proteins and nucleic acids (5–8). Biomolecular condensates are involved in diverse cellular functions (9–12) and have been shown, both theoretically (13, 14) and experimentally (15), to buffer protein concentrations. In binary LLPS systems (i.e., mixtures of one solute in a solvent), concentrations are buffered as the equilibrium concentrations of components within each phase are fixed by thermodynamics, even if the total concentrations of the system change. This implies that LLPS can implement a cellular concentration control mechanism (16) when the system is in static equilibrium. In multicomponent LLPS, concentration buffering occurs when the noise distribution of concentrations aligns with the tie lines of the LLPS phase diagram (13). Cells experience protein concentration fluctuations across a wide range of timescales, ranging from transcriptional bursts and translation/degradation, which occur in minutes to hours (17, 18), to the cell cycle, which can affect concentrations on the order of hours (19), and environmental inputs that can span any of these timescales (8) (Fig. 1*A*). Furthermore, these perturbation timescales can overlap resulting in complex concentration perturbation profiles (Fig. 1*B*). However, it remains unclear whether condensates can buffer fast perturbations as effectively as slow ones and how the effectiveness of buffering at different timescales depends on condensate properties, such as interaction strength or size.

A natural way to study such dynamical regulation is to use the framework of control theory. Control theory provides powerful methods for analyzing how systems respond to perturbations and maintain stability (20, 21). At its core is the principle of feedback: the comparison between a desired output and the actual system state to reduce error. Feedback control underlies both engineered systems, from thermostats to flight guidance (21–23), and natural systems, including bacterial chemotaxis (24), calcium homeostasis in mammals (25), and the resilience of insect societies (26). While control-theoretic analysis has been applied to homogeneous biochemical networks (27–29), its extension

Author contributions: L.d.M.-I. and T.C.T.M. designed research; L.d.M.-I. and T.C.T.M. performed research; and L.d.M.-I., T.-Y.D.T., C.A.W., and T.C.T.M. wrote the paper.

The authors declare no competing interest.

This article is a PNAS Direct Submission.



[1]To whom correspondence may be addressed. Email: thomas.michaels@bc.biol.ethz.ch.

This article contains supporting information online at https://www.pnas.org/lookup/suppl/doi:10.1073/pnas.2526810123/-/DCSupplemental.

Published July 30, 2026.

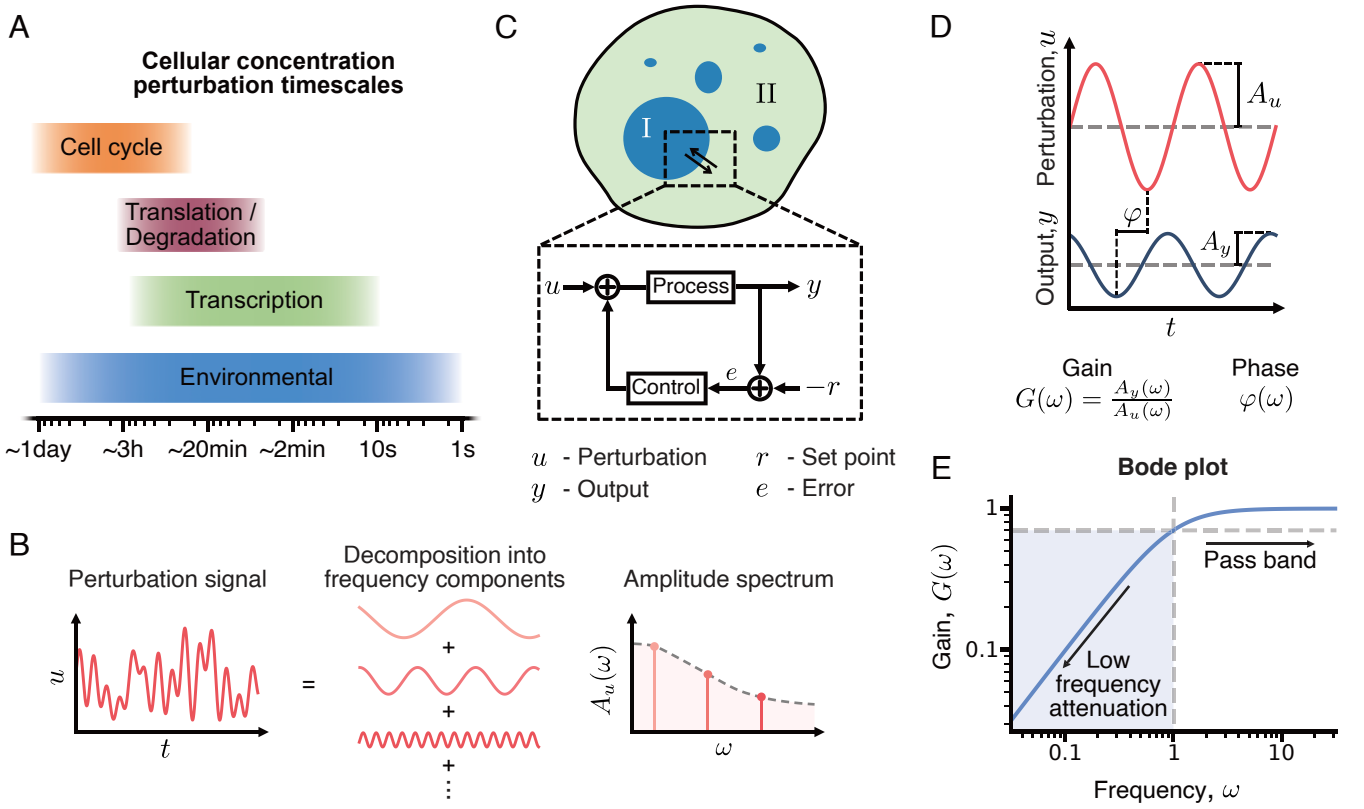


**Fig. 1.** Schematics of cellular concentration perturbations, LLPS-based feedback control and frequency response characterization. (*A*) Examples of cellular and environmental processes that change the concentrations of phase separating components across a wide range of timescales. (*B*) Cellular and environmental processes generate complex time-dependent concentration perturbations spanning multiple timescales. Such perturbations can be represented in terms of frequency components with different amplitudes (amplitude spectrum). This spectral decomposition motivates the use of Bode plots to characterize how LLPS attenuates or transmits fluctuations across frequencies. (*C*) Schematic of the LLPS feedback control system. A process produces an output concentration $y$ in phase I from an input concentration perturbation $u$ in phase II. We then measure the error, $e = y - r$, where $r$ is the desired concentration in phase I. The error is then operated on by a controller and added back to the input. (*D*) Schematic of a sinusoidal input $u$ and the output $y$ showing how the gain $G$ and phase shift $\varphi$ are measured. (*E*) Bode plots are constructed by varying the input frequency and measuring $G$ as a function of $\omega$. This schematic shows the behavior of a high-pass filter that attenuates low frequency perturbations and allows high frequencies to pass through.

to spatially heterogeneous systems such as biomolecular condensates has remained largely unexplored (16).

Here, we apply control theory to condensates to uncover the dynamic principles of concentration buffering. Using analytic modeling and simulations, we perform a systematic frequency-domain analysis of LLPS. We show that condensates act as frequency-selective filters, suppressing some frequencies of concentration fluctuations while transmitting others. By linking filtering behavior to LLPS parameters such as interaction strength and droplet size, we identify fundamental dynamical limits of condensate-mediated concentration buffering. These results suggest a mechanism for how phase separation could contribute to cellular robustness and offer design principles for engineering synthetic condensates with tunable control properties.

## Results

**Control Theory.** Control strategies can be broadly classified into two categories: open-loop control and closed-loop control (30, 31). Open-loop control employs static parameters optimized for specific conditions to minimize error, but it lacks adaptability to dynamic changes. In contrast, closed-loop control leverages feedback: It continuously measures the system error and adjusts inputs dynamically to bring the output closer to the set-point. For example, bacterial chemotaxis employs closed-loop control to adapt to changing concentrations of chemoattractants, ensuring robust directional movement (24, 32).

Closed-loop control operates by tracking the system error $e = y - r$, i.e., the difference between current system output $y$ and desired output $r$ (set point). The error is then processed through a controller that uses this information to adjust inputs and correct the error (Fig. 1*C*). The controller can perform various operations on the error to steer the system under control, for example, proportional-integral (PI) control (33, 34).

The characteristics of a control system are commonly analyzed using the frequency response of the system to test oscillatory input perturbations with a form $u(t) = A_u(\omega)\sin(\omega t)$ of varying frequency $\omega$. This approach is motivated by the fact that general time-dependent perturbations $u(t)$ can be represented in terms of frequency components with different amplitudes, quantified by their amplitude spectrum (Fig. 1*B*). For linear systems, the response to a complex perturbation $u(t)$ then follows from the superposition of the responses to its individual frequency components. For example, stochastic gene-expression dynamics generate protein concentration fluctuations with a frequency-dependent spectrum, $|A_u(\omega)|^2 \propto (\gamma^2 + \omega^2)^{-1}$ (35). Similarly, more complex intracellular processes, such as combinations of transcriptional bursts, translation/degradation and cell cycle progression, can generate protein concentration fluctuations with frequency-dependent amplitudes (35). To find the response to a given frequency component $\omega$, we measure the ratio of the output

amplitude $A_y(\omega)$ to the input amplitude $A_u(\omega)$, which is called the gain $G(\omega) = A_y(\omega)/A_u(\omega)$ (Fig. 1*D*). The phase shift $\varphi(\omega)$ measures the delay between the input and output signals. By varying the input frequency $\omega$ and measuring the gain $G(\omega)$ and the phase shift $\varphi(\omega)$, we can construct the full frequency response of the system, the so-called Bode plot (30, 36, 37) see Fig. 1*E* for an illustration. Bode plots characterize the performance of a feedback system, including filtering effects. Feedback systems can attenuate some frequencies of perturbations and allow others to pass through creating a frequency filter. Bode plots visualize this filtering effect by showing lower gain for attenuated frequencies and high gain for frequencies that pass through. For example, Fig. 1*E* depicts the Bode plot of a high-pass filter, where low frequency perturbations are attenuated but high frequencies can pass through.

In this paper, we perform a Bode plot analysis of LLPS concentration buffering to assess how phase separation attenuates or transmits different frequency components of intracellular concentration fluctuations. To this end, we build on theoretical work (14, 16, 38) to devise a simple model of a dynamic LLPS system and employ control theory analysis tools to characterize its control characteristics.

**Model of Phase-Separation Dynamics.** We consider a binary mixture consisting of a solvent ($i = 0$) and a solute ($i = 1$; e.g. a protein). Let $v_0$ and $v_1$ denote the molecular volumes of solvent and solute, respectively. Due to interactions between components, the system can undergo liquid–liquid phase separation (LLPS) into two coexisting phases: a solute-rich condensate phase (phase I) and a surrounding solute-poor dilute phase (phase II) (Fig. 1*C*). Rather than resolving spatial concentration fields, we adopt a coarse-grained "two-compartment" description in which each phase is characterized by its average composition and volume. This reduction is appropriate when intraphase relaxation (e.g. diffusion within each phase) is fast compared to interphase exchange across the interface (39, 40) (see *SI Appendix*, section S1.2 for a derivation). We denote by $N_i^{(\alpha)}(t)$ the particle number of component $i = 0, 1$ in phase $\alpha = \mathrm{I}, \mathrm{II}$ at time $t$ and by $V^{\mathrm{I}}(t)$ and $V^{\mathrm{II}}(t)$ the corresponding phase volumes. The total system volume is fixed, $V = V^{\mathrm{I}}(t) + V^{\mathrm{II}}(t)$, such that $V^{\mathrm{II}}(t) = V - V^{\mathrm{I}}(t)$. In cells, condensates can occupy varying fractions of the available cyto- or nucleoplasmic volume. For example, P granules in *Caenorhabditis elegans* embryos occupy a small fraction of the cytoplasm, with estimated fractional volumes $V^{\mathrm{I}}/V \sim 10^{-4}$ to $10^{-3}$ (8). For stress granules, reported droplet diameters of 0.1 to 2 μm and typical abundances of 10 to 100 condensates per stressed cell yield estimated cytoplasmic volume fractions $V^{\mathrm{I}}/V \sim 10^{-5}$ to $10^{-2}$ (41). In the nucleus, chromocenters can occupy up to around 5% of nuclear volume in mammalian cells (42). Nucleoli represent one of the largest intracellular condensates: In yeast, they can occupy up to ∼20% of the nuclear volume (43), while estimates for HeLa cells based on reported nucleolar diameters (1 to 5 μm) and copy numbers (2 to 5 nucleoli per nucleus) give $V^{\mathrm{I}}/V \sim 10^{-3}$ to $10^{-1}$ (44).

To describe the system's dynamics, we formulate a set of coupled ordinary differential equations (ODEs) governing the volume fraction of component $i = 0, 1$ in each phase, defined as $\phi_i^{\mathrm{I/II}}(t) = v_i N_i^{\mathrm{I/II}}(t)/V^{\mathrm{I/II}}(t)$,* as well as the condensate volume $V^{\mathrm{I}}(t)$. These variables evolve due to interphase exchange:

*Note that volume fractions $\phi_i^{\mathrm{I/II}}$ are related to the concentrations $c_i^{\mathrm{I/II}}$ of component $i$ in phases I, II through $\phi_i^{\mathrm{I/II}} = v_i c_i^{\mathrm{I/II}}$.

We define $J_i(t)$ as the net exchange rate of species $i$ across the interface (units: particles per unit time), taken positive when particles are transferred from phase I to phase II. Mass conservation across the interface implies that the same exchange rate appears with opposite sign in the two phases. The total amount of the solute component 1 in the system can fluctuate due to synthesis, degradation, or external perturbations, but phase separation dynamically redistributes components between the two phases, allowing the system to buffer changes in concentration after a perturbation. Applying particle conservation in each phase, together with the relation between particle number, volume fraction, and phase volume, yields the following coupled ODEs (see *SI Appendix*, section S1.1 for a detailed derivation):

$$\frac{d\phi_1^{\mathrm{I}}(t)}{dt} = -\frac{v_1 J_1(t)}{V^{\mathrm{I}}(t)} + \frac{\phi_1^{\mathrm{I}}(t)}{V^{\mathrm{I}}(t)}\frac{dV^{\mathrm{I}}(t)}{dt}, \qquad [1a]$$

$$\frac{d\phi_1^{\mathrm{II}}(t)}{dt} = \frac{v_1 J_1(t)}{V - V^{\mathrm{I}}(t)} - \frac{\phi_1^{\mathrm{II}}(t)}{V - V^{\mathrm{I}}(t)}\frac{dV^{\mathrm{I}}(t)}{dt}, \qquad [1b]$$

$$\frac{dV^{\mathrm{I}}(t)}{dt} = -v_0 J_0(t) - v_1 J_1(t), \qquad [1c]$$

where we used $V^{\mathrm{II}}(t) = V - V^{\mathrm{I}}(t)$ and the solvent volume fraction is not an independent variable but is determined by $\phi_0^{\mathrm{I/II}}(t) = 1 - \phi_1^{\mathrm{I/II}}(t)$, so no separate evolution equation for the solvent is required.

Eq. **1** provide a coarse-grained dynamical description of LLPS in terms of the phase compositions $\phi_1^{\mathrm{I/II}}$, the condensate volume $V^{\mathrm{I}}$, and the interphase exchange rates $J_i$. Their physical interpretation is straightforward. The first two equations describe how the solute volume fractions in the dense and dilute phases change due to interfacial exchange. In each phase, the solute composition evolves both because particles are transferred across the interface and because changes in the condensate volume dilute or concentrate the solute. The third equation governs the evolution of the condensate volume. It enforces incompressibility by relating changes in $V^{\mathrm{I}}$ to the net exchange of solvent and solute across the interface. Because the total system volume is fixed, any transfer of material between phases must be accompanied by a corresponding redistribution of phase volumes.

To close the system of equations, we must specify constitutive relations for the interphase exchange rates $J_i$ in terms of the variables $\phi_1^{\mathrm{I/II}}$ and $V^{\mathrm{I}}$. In the linear-response regime, appropriate for small deviations from phase equilibrium, we assume that the exchange rate of each species is proportional to the corresponding chemical potential difference between phases (38, 45)

$$v_i J_i = L_i(\mu_i^{\mathrm{I}} - \mu_i^{\mathrm{II}}), \qquad [2]$$

where $\mu_i^{\alpha}$ is the chemical potential of species $i = 0, 1$ in phase $\alpha = \mathrm{I}, \mathrm{II}$, and the mobility coefficients $L_i$ set the characteristic timescale of interphase exchange. To relate these coefficients to physically measurable quantities, we estimate $L_i$ by matching Eq. **2** to continuum descriptions of interfacial transport for a spherical droplet of radius $R$, yielding $L_1 \simeq \frac{R\,\phi_{1,\mathrm{eq}}^{\mathrm{I}}}{k_B T\,\tau_{\mathrm{ex}}}$ (*SI Appendix*, section S1.3) (39). Here, $\tau_{\mathrm{ex}}$ is the characteristic exchange time, which can be estimated as $\tau_{\mathrm{ex}} \simeq \frac{R^2}{\pi D^{\mathrm{I}}} + \frac{\phi_{1,\mathrm{eq}}^{\mathrm{I}} R^2}{3\,\phi_{1,\mathrm{eq}}^{\mathrm{II}} D^{\mathrm{II}}} + \frac{R}{3\sigma}$, where $D^{\mathrm{I}}$ and $D^{\mathrm{II}}$ are the diffusion coefficients of solute molecules in the dense and dilute phases, respectively, $\phi_{1,\mathrm{eq}}^{\mathrm{I}}$ and $\phi_{1,\mathrm{eq}}^{\mathrm{II}}$ are the corresponding equilibrium solute volume fractions, and $\sigma$

is the interfacial conductance (39). As we use a phase averaged model that assumes that intraphase relaxation is fast compared to interphase exchange, $\tau_{ex}$ sets the upper frequency limit of applicability of the theory.

The chemical potential $\mu_i = \partial F/\partial N_i$ of each component $i$ is obtained from the derivative of the free energy $F$ of the system with respect to particle number $N_i$. To compute the interphase exchange rates $J_i$, we therefore require an explicit thermodynamic model for LLPS. Here, we employ the Flory–Huggins model, a widely used and well-established framework for describing phase separation in polymer mixtures (46–48). We note that our results are qualitatively robust to the choice of $F$ and thus other LLPS models can be used for this control analysis (49, 50). In the Flory–Huggins model, the free energy density is given by

$$\frac{F}{V} = \frac{k_B T}{\nu_0}\left[\phi_0 \ln \phi_0 + \phi_1 \ln \phi_1 + \chi\, \phi_0\, \phi_1\right], \qquad [3]$$

where we set $\nu_0 = \nu_1$ for simplicity. In this model, phase separation arises from a competition between entropic contributions, which favor mixing, and enthalpic interactions, encoded by the Flory interaction parameter $\chi$, which favor demixing. When $\chi$ exceeds the critical value $\chi_c = 2$, the homogeneous mixture becomes unstable and separates into coexisting dense and dilute phases. The equilibrium compositions of the two phases, $\phi^{\mathrm{I}}_{1,\mathrm{eq}}$ and $\phi^{\mathrm{II}}_{1,\mathrm{eq}}$, are determined by the condition of chemical equilibrium, $\mu^{\mathrm{I}}_i = \mu_i\left(\phi^{\mathrm{I}}_{1,\mathrm{eq}}\right) = \mu_i\left(\phi^{\mathrm{II}}_{1,\mathrm{eq}}\right) = \mu^{\mathrm{II}}_i$. Here, we neglect surface tension effects: For biomolecular condensates such as P granules, the capillary length has been estimated to be on the nanometer scale, whereas typical droplet radii are on the micrometer scale, implying that Laplace-pressure corrections to phase compositions are negligible (8).

Having defined the basic equations for LLPS dynamics, we now consider the effect of concentration perturbations of the phase-separating species. For illustration purposes, we focus on perturbations occurring in the dilute phase, which mimics biologically relevant scenarios such as phase separating proteins undergoing transcriptional bursting occurring primarily in the surrounding cytoplasm (18) or active intracellular transport between the nucleoplasm and cytoplasm (51), but note that perturbations applied to the dense phase or to both phases can be treated within the same framework.

This is captured by extending Eq. **1** as

$$\frac{d\phi^{\mathrm{II}}_1}{dt} = \frac{\nu_1 J_1}{V^{\mathrm{II}}} - \frac{\phi^{\mathrm{II}}_1}{V^{\mathrm{II}}}\frac{dV^{\mathrm{I}}}{dt} + \frac{du}{dt}, \qquad [4]$$

where $du/dt$ denotes a perturbation flux of component 1 in the dilute phase. The perturbation enters as a time derivative so that $u(t)$ represents a direct perturbation to the composition rather than a perturbation in particle flux. The resulting formulation allows us to probe how LLPS dynamically filters time-dependent concentration fluctuations. Full mathematical details and derivations are provided in *SI Appendix*.

**Frequency Analysis and Bode Plots for Binary LLPS.** Due to the nonlinearity of the dynamical equations in Eq. **1**, we first perform a numerical frequency–response analysis. Following the Bode plot recipe detailed in *Control Theory*, we perturb the LLPS system with a test oscillatory volume-fraction perturbation of the form $u(t) = A_u(\omega)\sin(\omega t)$. We numerically solve the resulting system of ODEs over a wide range of driving frequencies $\omega$. For each frequency $\omega$, we apply a fast Fourier transform (FFT) to the resulting time series of volume fractions, thereby converting from the time domain to the frequency domain (*SI Appendix*, section S2.1 and Fig. S1). From the FFT spectrum, we extract the complex Fourier component at the driving frequency $\omega$ and take its modulus and argument to obtain the output amplitude $A_y(\omega)$ and phase shift $\varphi_y(\omega)$ of the volume-fraction response, respectively. Here, the output variable $y(t)$ corresponds to the solute volume fraction in a given phase, either $\phi^{\mathrm{I}}_1(t)$ or $\phi^{\mathrm{II}}_1(t)$. The phase shift quantifies the delay of the output response to the input perturbation. The gain is then defined as the ratio of the output amplitude to the input amplitude, $G(\omega) = \frac{A_y(\omega)}{A_u(\omega)}$, which quantifies how strongly an imposed perturbation in the dilute phase is transmitted to volume-fraction fluctuations in each phase. We distinguish between the gains $G^{\mathrm{I}}(\omega)$ and $G^{\mathrm{II}}(\omega)$, corresponding to the responses of the dense and dilute phases, respectively. Note that, for a system in the linear regime, the output amplitude is proportional to the input amplitude. Hence, their ratio (the gain) is intrinsic to the system and does not depend on the specific choice of $A_u(\omega)$.

To obtain analytical insight into how phase separation dynamically buffers concentration perturbations, we analyze the linearized LLPS dynamics using tools from linear control theory. By linearizing the kinetic equations (Eq. **1**) around phase equilibrium, we obtain a tractable analytical framework that allows us to connect the frequency response directly to phase-separation parameters. For linear systems, the frequency domain is accessed by taking the Laplace transform of the system (30). This approach allows us to derive explicit transfer functions that relate externally imposed concentration perturbations to the resulting responses of the dense and dilute phases in the frequency domain. For the binary LLPS system defined by Eq. **1**, we collect the dynamical variables into the output vector $\boldsymbol{y}(t) = \left(\phi^{\mathrm{I}}_1(t), \phi^{\mathrm{II}}_1(t), V^{\mathrm{I}}(t)\right)^T$, which comprises the solute volume fractions in the dense and dilute phases, together with the condensate volume. The system is then subjected to an externally imposed perturbation in the dilute phase only, represented as $\boldsymbol{u}(t) = \boldsymbol{b}\,u(t)$, where $u(t)$ is a general scalar perturbation to the dilute-phase solute volume fraction and $\boldsymbol{b} = (0,1,0)^T$. This choice mimics the scenario in which concentration fluctuations arise primarily in the surrounding cytoplasm (e.g., from synthesis or degradation), although the framework can be straightforwardly extended to perturbations in either phase. With this notation, the perturbed nonlinear LLPS dynamics can be written compactly as $\dot{\boldsymbol{y}} = \boldsymbol{F}(\boldsymbol{y}) + \boldsymbol{b}\,\dot{u}$, where $\boldsymbol{F}(\boldsymbol{y})$ represents the right-hand side of Eq. **1**. Linearizing the dynamics around the phase-equilibrium set point $\boldsymbol{r} = \left(\phi^{\mathrm{I}}_{1,\mathrm{eq}}, \phi^{\mathrm{II}}_{1,\mathrm{eq}}, V^{\mathrm{I}}_{\mathrm{eq}}\right)^T$, and defining the error $\boldsymbol{e}(t) = \boldsymbol{y}(t) - \boldsymbol{r}$, yields

$$\dot{\boldsymbol{e}} = \boldsymbol{J}\,\boldsymbol{e} + \boldsymbol{b}\,\dot{u}, \qquad [5]$$

where $\boldsymbol{J} = \left.\frac{\partial \boldsymbol{F}}{\partial \boldsymbol{y}}\right|_{\boldsymbol{r}}$ is the Jacobian matrix of the LLPS dynamics evaluated at phase equilibrium. To analyze the system's response in the frequency domain, we take the Laplace transform of the linearized equations (Eq. **5**), yielding:

$$\hat{\boldsymbol{e}}(s) = s\,(s\boldsymbol{I} - \boldsymbol{J})^{-1}\boldsymbol{b}\,\hat{u}(s), \qquad [6]$$

where $\hat{f}(s) = \int_0^\infty f(t)e^{-st}dt$ denotes the Laplace transform of $f(t)$. This expression captures the dynamic response to perturbations and defines a vector-valued transfer function

$\boldsymbol{H}(s) = s(s\boldsymbol{I} - \boldsymbol{J})^{-1}\boldsymbol{b}$ from the scalar perturbation $u$ to the system outputs $\boldsymbol{y}$. The three components of $\boldsymbol{H}(s)$ are the scalar transfer functions from the perturbation $u$ to the outputs $\phi_1^{\mathrm{I}}$, $\phi_1^{\mathrm{II}}$, and $V^{\mathrm{I}}$, respectively. Since our focus is on concentration buffering, we consider only the first two components, $H^{\mathrm{I}}(s)$ and $H^{\mathrm{II}}(s)$, which describe the output-to-disturbance transfer functions for compositions in each phase, yielding (see *SI Appendix*, section S2.2 for a derivation):

$$H^{\mathrm{I}}(s) = \frac{K_g s}{s^2 + K_p s + K_i}, \quad [7]$$

$$H^{\mathrm{II}}(s) = \frac{s^2 + K_h s}{s^2 + K_p s + K_i}, \quad [8]$$

where $K_p$, $K_i$, $K_g$, and $K_h$ are functions of the equilibrium phase compositions, condensate volume, and interphase exchange kinetics. Explicit expressions linking these coefficients to LLPS parameters are provided in *SI Appendix*.

To analyze the system's frequency response, we construct Bode plots by substituting $s = i\omega$ into Eqs. **7** and **8** ($i$ denotes here the imaginary unit) and obtaining the frequency-dependent gains for the dense and dilute phases as the moduli of the corresponding transfer functions, $G^{\alpha}(\omega) = \left|H^{\alpha}_{\mathrm{od}}(i\omega)\right|$, $\alpha = \mathrm{I}, \mathrm{II}$ (see *SI Appendix*, section S2.2 for derivation)

$$G^{\mathrm{I}}(\omega) = \frac{|K_g|\,\omega}{\sqrt{(K_i - \omega^2)^2 + K_p^2\,\omega^2}}, \quad [9]$$

$$G^{\mathrm{II}}(\omega) = \frac{\omega\sqrt{\omega^2 + K_h^2}}{\sqrt{(K_i - \omega^2)^2 + K_p^2\,\omega^2}}. \quad [10]$$

The corresponding phase shifts are given by $\varphi^{\alpha}(\omega) = \arg[H^{\alpha}(i\omega)]$, $\alpha = \mathrm{I}, \mathrm{II}$.

The resulting Bode plots for the gains $G^{\mathrm{I/II}}(\omega)$ and phase shifts $\varphi^{\mathrm{I/II}}(\omega)$ computed numerically and using the analytical transfer functions are shown in Fig. 2 and reveal distinct filtering behavior in the two phases. In the perturbed dilute phase (phase II), the solute volume fraction $\phi_1^{\mathrm{II}}$ exhibits a high-pass–like response: Slow perturbations are strongly attenuated, while at sufficiently high frequencies the gain approaches unity, indicating that rapid forcing is transmitted directly to the dilute phase when interphase exchange cannot respond. In contrast, the dense phase displays a band-pass response, attenuating both high and low frequency perturbations. At low frequencies, the gain $G^{\mathrm{I}}(\omega)$ vanishes, reflecting effective buffering as interfacial exchange and volume redistribution have sufficient time to restore phase equilibrium. At high frequencies, the gain again decays, because exchange dynamics are too slow to track rapid perturbations.

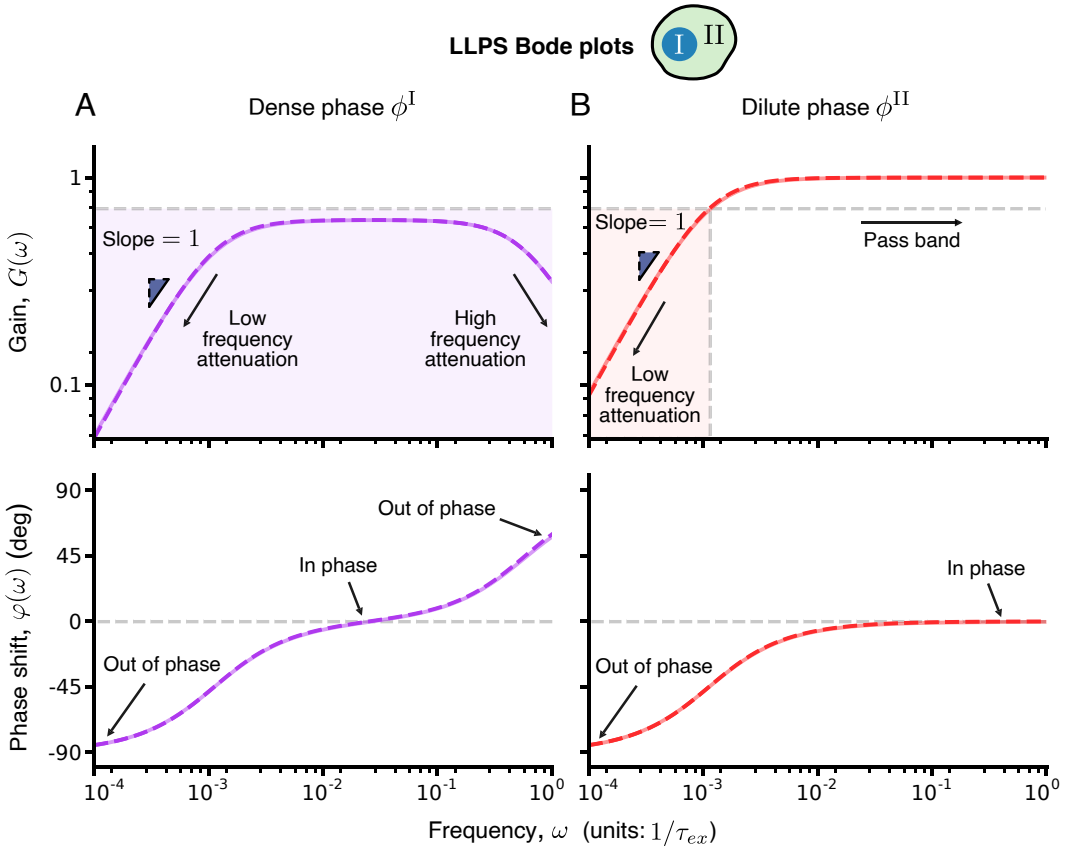


**Fig. 2.** Bode plots showing the frequency response $G^{\mathrm{I/II}}(\omega)$ and $\varphi^{\mathrm{I/II}}(\omega)$ of binary LLPS to concentration perturbations in the dilute phase. The frequency-domain analysis shows distinct filtering properties in each phase: The dense phase (*A*) attenuates both slow and fast fluctuations, whereas the dilute phase (*B*) acts as a high-pass filter, transmitting fast perturbations while suppressing slow ones. Dotted lines are Bode plots obtained from the numerical method and solid lines are from the analytical method showing very close agreement. The LLPS parameters for both plots were $\chi = 2.179$, and $V_{\mathrm{eq}}^{\mathrm{I}}/V = 3 \times 10^{-3}$. For the numerical method we choose $|A_u(\omega)|^2 = 2k/(\gamma^2 + \omega^2)$, which we use as an example amplitude spectrum from gene expression fluctuations with $2k = 10^{-8}$ and $\gamma^2 = 10^{-2}$, but note that the resulting Bode plots are independent of the specific choice of the frequency dependence of $A_u(\omega)$ provided that the magnitude of $A_u(\omega)$ is small enough for the linear regime to hold. The frequencies are normalized to the characteristic interphase exchange time $\tau_{\mathrm{ex}}$, so a normalized frequency of 1 is equal to $1/\tau_{\mathrm{ex}}$. Frequencies do not exceed $1/\tau_{\mathrm{ex}}$ such that the phase averaged model is valid.

As a consequence, $G^{\mathrm{I}}(\omega)$ exhibits a single maximum at an intermediate frequency $\omega^\star = \sqrt{K_i}$, corresponding to the frequency at which buffering is least effective. The peak frequency $\omega^\star$ is proportional to the inverse of the characteristic interphase exchange time $1/\tau_{\mathrm{ex}}$ times a prefactor depending on $V^{\mathrm{I}}$ and $\chi$. Thus the timescale of low-frequency attenuation is set by the characteristic interphase exchange time $\tau_{\mathrm{ex}}$. Reported exchange measurements for in vitro FUS droplets place $\tau_{\mathrm{ex}}$ on the order of seconds (52). Using our Bode plot framework, we would expect the low-frequency concentration attenuation of the FUS droplets to be on the order of minutes$^{-1}$ or lower and high-frequency attenuation at seconds$^{-1}$. This implies a characteristic cutoff frequency: Perturbations with $\omega \ll \omega^\star$ are strongly buffered, whereas faster inputs ($\omega \gtrsim \omega^\star$) are increasingly transmitted in the dilute phase. This mapping is consistent with experiments demonstrating concentration buffering at (quasi)steady state (15), a regime corresponding to $\omega \to 0$ in our theory. Conversely, our analysis predicts reduced buffering efficacy for rapid perturbations (e.g. fast input pulses or shocks), particularly when exchange is slowed by interfacial barriers (39) or when the interaction parameter is small, which together shift $\omega^\star$ to lower values. Because condensate size, material properties, and exchange kinetics vary widely across systems (39, 52, 53), the frequency window over which buffering is effective is expected to be system specific and tunable.

The phase shifts $\varphi^{\mathrm{I/II}}(\omega)$ provide additional insight into the dynamical response. At low frequencies, both phases exhibit a phase shift of $-90°$, indicating that composition changes arise from the slow accumulation of material through interphase exchange, consistent with quasi-static equilibration. In the dense phase, the phase shift increases toward 0° near the frequency where the gain is maximal, reflecting the regime in which condensate composition most directly tracks external perturbations. At higher frequencies, the phase shift of the dense phase approaches 90°, indicating that exchange and volume relaxation are too slow to respond and that the dense phase becomes effectively decoupled from rapid forcing. By contrast, the dilute phase transitions from $-90°$ at low frequencies to 0° at high frequencies, reflecting a crossover from exchange-dominated dynamics to direct tracking of the imposed perturbation.

**Connecting LLPS Parameters and Control Properties.** By embedding our model of phase separation into a control-theoretical framework, we establish a direct quantitative connection between the thermodynamic and kinetic parameters of LLPS and the disturbance rejection properties of biomolecular condensates. Specifically, we use Bode plots obtained from the analytical transfer functions (Fig. 3) to explore how key parameters, including interaction strength and phase volume, shape the frequency response of the system by tuning the coefficients $K_p$, $K_i$, $K_h$, and $K_g$.

We first examine the role of the interaction parameter $\chi$, which quantifies the competition between demixing interactions and mixing entropy (Fig. 3*A*). Decreasing $\chi$ weakens phase separation and reduces the contrast between the coexisting phases. Analytically, this corresponds to the limit $\chi \to \chi_c$, where the coefficients $K_p$ and $K_i$ vanish. As a result, both the peak frequency $\omega^\star$ and the low-frequency attenuation scale collapse, and the gain curve shifts to lower frequencies. In the critical limit $\chi \to \chi_c$, the two-phase regime disappears entirely and the dense phase loses its ability to buffer slow perturbations. This demonstrates that robust low-frequency attenuation is a direct dynamical consequence of phase separation itself. Biologically,

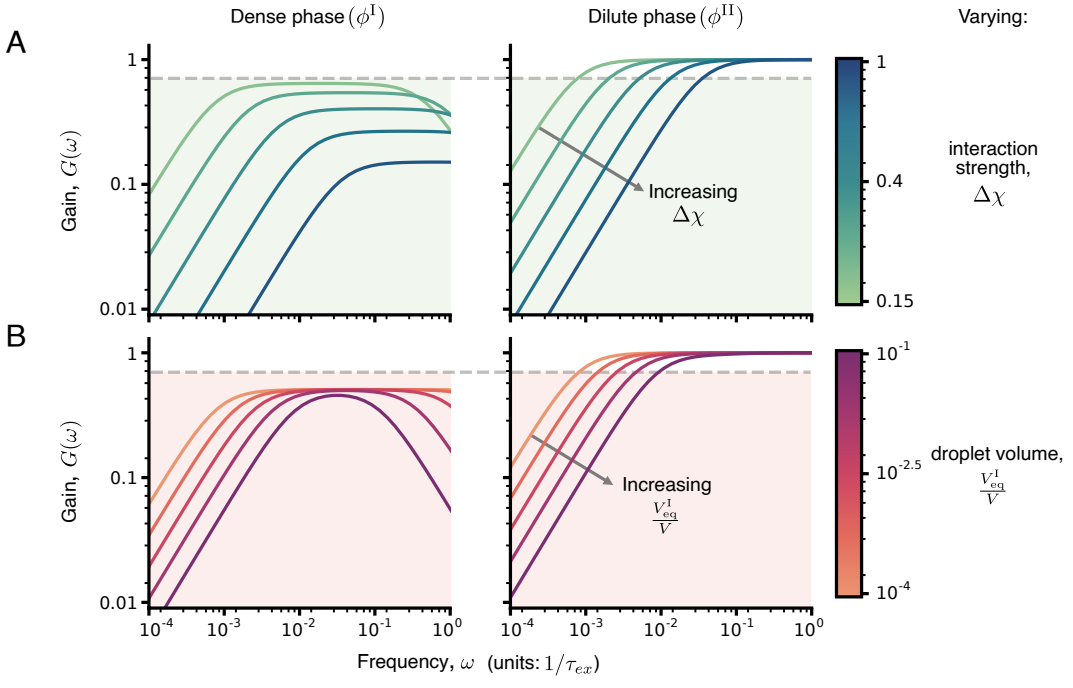


**Fig. 3.** Bode plots under varying LLPS parameters. (*A*) Effect of the interaction parameter $\chi$ above the critical point ($\Delta\chi = \chi - \chi_c$) and (*B*) effect of the droplet volume $V^{\mathrm{I}}_{\mathrm{eq}}/V$. Increasing interaction strength or droplet volume broadens the frequency range over which perturbations are attenuated, whereas weaker interactions or smaller condensates reduce buffering efficacy. Parameters for all plots are $\Delta\chi = 0.274$, $V^{\mathrm{I}}_{\mathrm{eq}}/V = 3 \times 10^{-3}$ except when a specific parameter is changed. In increasing order: (*A*) $\Delta\chi = 0.15, 0.24, 0.39, 0.62, 1.0$; (*B*) $V^{\mathrm{I}}_{\mathrm{eq}}/V = 0.0001, 0.00056, 0.0032, 0.018, 0.1$. As with Fig. 2, the frequencies are in units of the reciprocal of the characteristic interphase exchange time $1/\tau_{\mathrm{ex}}$.

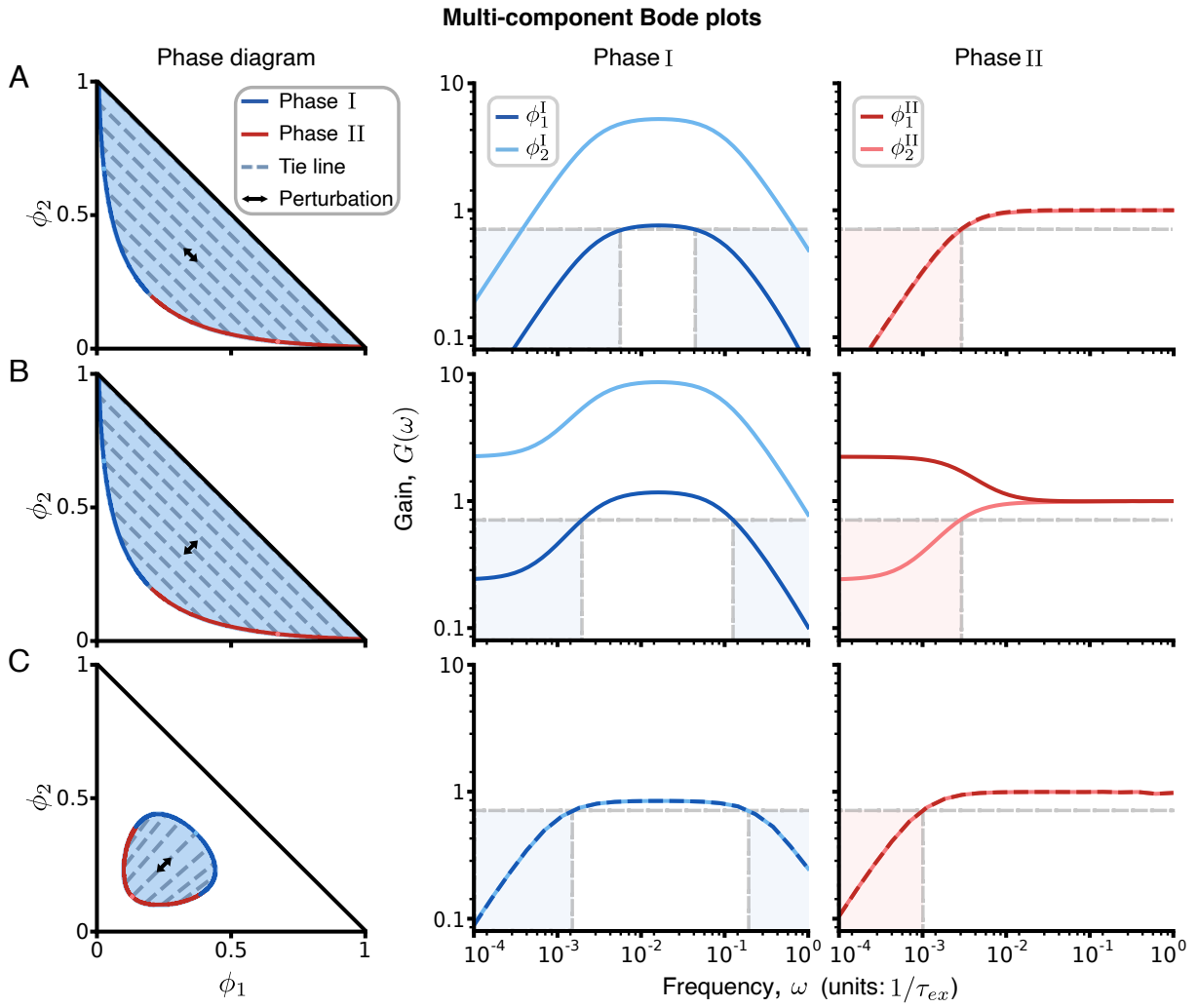


**Fig. 4.** Bode plots for multicomponent LLPS with two exchanging solutes. (*A* and *B*) Bode plots for a three-component segregative LLPS system. In panel (*A*), phase II is perturbed by exchanging component 1 for component 2 at equal stoichiometric ratio, corresponding to perturbations along a tie line (black arrow). In panel (*B*), components 1 and 2 are exchanged equally with the solvent, producing perturbations that change the tie line. In the accompanying phase diagrams, red and blue curves denote the binodal coexistence compositions of the two phases, and dashed tie lines connect coexisting equilibrium states. (*C*) Bode plot for associative LLPS, where the dense phase is enriched in both components. The perturbation is identical to panel (*B*), but now lies along a tie line. Phase diagrams and Bode plots are obtained numerically from a three-component Flory–Huggins free energy density $f = \frac{k_B T}{v_0}(\phi_0 \ln\phi_0 + \phi_1 \ln\phi_1 + \phi_2 \ln\phi_2 + \chi_{12}\phi_1\phi_2)$ with and $\chi_{12} = 5$ (*A* and *B*) and $\chi_{12} = -8.7$ (*C*). The remaining parameters used are $V_{\mathrm{eq}}^{\mathrm{I}}/V = 3 \times 10^{-3}$ and $A_u = 0.0005$ for all Bode plots. In line with the previous Bode plots, the frequencies have units of $(1/\tau_{\mathrm{ex}})$.

this implies that condensates operating close to criticality are less effective at buffering long-timescale concentration changes. In contrast, for strong phase separation ($\chi \gg \chi_c$), the analytical expressions show that $K_i$, $K_p$ and $K_h$ grow rapidly with $\chi$ while $K_g$ saturates, leading to an increase in the characteristic frequency $\omega^\star$ and a strong suppression of the peak gain. Consequently, increasing $\chi$ shifts the band-pass peak of the dense phase to higher frequencies while simultaneously reducing its amplitude, corresponding to more effective buffering over a broader range of timescales.

Next, we analyze the effect of the equilibrium droplet volume $V_{\mathrm{eq}}^{\mathrm{I}}$ (Fig. 3*B*). Larger droplets lead to a lower maximum gain in the dense phase, reflecting their increased capacity to absorb and redistribute solute. At the same time, increasing $V_{\mathrm{eq}}^{\mathrm{I}}$ shifts the characteristic frequency $\omega^\star$ to lower values, extending effective buffering to slower perturbations. In the dilute phase, a larger dense phase acts as a stronger sink, enhancing attenuation of low-frequency perturbations by enabling slower, exchange-mediated redistribution over longer timescales.

**Multicomponent LLPS Frequency Analysis.** So far, we have considered binary LLPS. Typically, however, condensates in vivo contain many components that interact with each other giving more complex phase behavior (7, 10). For example, for 3-component LLPS (2 solutes and a solvent), repulsive interactions give rise to segregative LLPS with two phases that are dense in one of the solutes (Fig. 4*A*). Associative LLPS occurs when the two solutes are attractive, making a phase dense in both (Fig. 4*C*). However, unlike 2-component phase separation, changing total volume fractions can change equilibrium concentrations, making the effectiveness of buffering also depend on the way the composition changes (13, 14). This raises the question of how introducing more components affects the ability for condensates to dynamically concentration buffer.

To this end, we extend our dynamic model and frequency analysis methods to multicomponent LLPS (*SI Appendix*, section S3). In a multicomponent condensate with $M$ solutes, the linearized composition dynamics have dimension $2M$, leading to additional relaxation modes compared to the binary case. Each

mode corresponds to a collective interfacial exchange pattern involving one or more species across the two coexisting phases. As we show in *SI Appendix*, section S3, the resulting transfer functions for the composition of species $j = 1, \cdots, M$ in phase $\alpha = \mathrm{I}, \mathrm{II}$ admit a modal expansion of the form

$$H_j^\alpha(s) = \sum_k \frac{s\, r_{jk}^\alpha}{s - \lambda_k}, \qquad [11]$$

where the eigenvalues $\lambda_k$ of the linearized dynamics set characteristic timescales and the residues $r_{jk}^\alpha$ encode how a given perturbation excites each mode and how it appears in a chosen output. Consequently, coupling between species can broaden or split the frequency range over which buffering occurs, and different components can exhibit distinct filtering behavior. We illustrate this behavior with three representative examples for 3-component LLPS. First, we simulate a segregative system and add a perturbation to phase II that exchanges components 1 and 2 at an equal stoichiometric ratio (Fig. 4*A*). The resulting frequency response (Fig. 4*A*) shows similar behavior to the binary case with the unperturbed phase I having both high and low frequency filtering behavior and phase II only filtering lower frequencies. However, each component filters differently in each phase and additional modes in the dynamics add regions of amplification (gain $> 1$). In this case, the perturbation was added in such a way that the phase equilibria had constant volume fractions, so similar behavior to the binary case is expected. We then simulate the same system, but we change the perturbation so that components 1 and 2 are instead exchanged with the solvent (Fig. 4*B*). The frequency response to this orthogonal perturbation is drastically different, with any filtering effects at low frequencies reduced. Now the binodal equilibria change with the perturbation which can mean a small change in the volume fraction of one component can have a larger change in another. This is reflected in $\phi_1^{\mathrm{I}}$ and $\phi_2^{\mathrm{II}}$ being attenuated and $\phi_2^{\mathrm{I}}$ and $\phi_1^{\mathrm{II}}$ being amplified. However, when we change the system to be associative with a phase dense in both components we recover the filtering effects (Fig. 4*C*). This corroborates previous theoretical studies that the buffering ability of multicomponent LLPS strongly depends on the stoichiometry of the components and on the specific interactions between the components (13).

## Discussion

Our results show that concentration buffering by biomolecular condensates is inherently dynamic and constrained by timescales. While condensates are often described as stabilizing intracellular environments, we show that this stabilization depends critically on the relative frequency of fluctuations and on condensate properties such as size and interaction strength. Recognizing these dynamical limits provides a perspective on condensate function in cells, where fluctuations span timescales from seconds to hours, and suggests that phase separation may be tuned to filter specific ranges of perturbations rather than universally filter fluctuations.

Our analysis reveals that condensates exhibit distinct frequency-dependent filtering properties in each coexisting phase. In the dilute phase, where the perturbation is introduced, we observe a high-pass filter behavior: low-frequency perturbations are strongly attenuated, while high-frequency perturbations are transmitted. In contrast, the dense phase behaves as a band-stop filter, attenuating both low- and high-frequency perturbations. This suggests that the phase boundary itself contributes to an effective filtering mechanism, potentially adding an additional layer of regulation to the dynamics of macromolecular concentrations. We base these conclusions under the limitations of our spatially coarse-grained model which averages over diffusive effects within each phase, neglecting surface tension effects. Analytical control analysis is formally valid for small perturbations around equilibrium.

Importantly, we find that the filtering characteristics are tunable and depend on key thermodynamic parameters of LLPS. When the interaction strength $\chi$ approaches the critical value $\chi_c$, the condensate loses its ability to attenuate low-frequency perturbations. Conversely, strong interactions enhance low-frequency disturbance rejection, suggesting that phase separation is key to filtering slow fluctuations. In biological systems, interaction strength could be modulated by mutations or posttranslational modifications that alter multivalent binding affinity, as shown for RNA-binding proteins such as FUS and other prion-like domain–containing proteins (5, 9, 54, 55). Such tunability provides a mechanism by which cells could adapt the frequency range of concentration buffering to distinct physiological conditions.

In addition to interaction strength, other condensate properties such as droplet size and interphase exchange rates also modulate dynamic buffering. Larger droplets filter more effectively at low frequencies because of an increased ability to exchange with the dilute phase, whereas smaller droplets transmit fluctuations more readily and have a larger pass band. In cells, condensate size is highly variable and can be regulated by protein concentration, nucleation kinetics, or coalescence dynamics (5, 6, 44).

Bode plots, widely used in engineering and physical sciences, provide an intuitive and quantitative method to characterize such control properties. They are broadly applied to physical systems, from flight control systems (23) and how pilots interact with them (56) to battery design (57, 58), and are increasingly being applied in biology, including neural dynamics (59, 60), signaling cascades (61), and synthetic gene circuits (62, 63). Our work extends this methodology to LLPS, offering a framework to probe the dynamic regulation of biomolecular condensates. We anticipate that this type of control-theoretical analysis will be broadly applicable to study the dynamics of other LLPS-driven systems, including stress granules (64, 65), nucleolar dynamics (44), and transcriptional condensates (66).

Finally, to experimentally validate our predictions, we propose an in vitro assay using a well-characterized phase-separating protein such as G3BP1 or LAF-1 (65, 67). Fluorescently tagging the protein with a reporter protein can provide estimates of the protein concentration within the droplet by fluorescence methods. A microfluidic device can couple direct imaging of a droplet with controlled input of protein concentration so that a sinusoidal concentration profile can flow over a constrained droplet (68), analogous to the theoretical method of Bode plot construction. The construction of experimental Bode plots would offer a direct test of the dynamic filtering properties of condensates and reveal how physical parameters shape their control function in biological contexts.

## Materials and Methods

The ordinary differential equation (ODE) system describing the LLPS dynamics (Eq. **1**) was formulated using a phase-averaged model, with exchange fluxes modeled via linear-response theory. Numerical frequency analyses were performed by integrating the perturbed ODE system using the Radau method and accessing the frequency domain using the fast Fourier transform algorithm

(FFT). Both the numerical integration and FFT were computed using readily available functions of the SciPy library for Python. Analytical control analysis consisted of linearizing the ODE system around phase equilibrium and using control theory to derive transfer functions from which Bode plots could be obtained. A more detailed description of the system derivation, numerical method and control analysis are available in *SI Appendix*.

**Data, Materials, and Software Availability.** There are no data underlying this work.

**ACKNOWLEDGMENTS.** We thank Christoph Zechner and Anne-Lena Moor for useful discussions. This work was supported by ETH Zurich (L.d.M.-I. and T.C.T.M.), the Swiss NSF (Grant No. SNSF 219703 to T.C.T.M.).

Author affiliations: [a]Department of Biology, Institute of Biochemistry, ETH Zurich, Zurich 8093, Switzerland; [b]Bringing Materials to Life Initiative, ETH Zurich, Zurich 8093, Switzerland; [c]Department of Synthetic Biology, University of Saarland, Saarbrücken 66123, Germany; and [d]Faculty of Mathematics, Natural Sciences, and Materials Engineering, Institute of Physics, University of Augsburg, Augsburg 86159, Germany

1. M. B. Elowitz, A. J. Levine, E. D. Siggia, P. S. Swain, Stochastic gene expression in a single cell. *Science* **297**, 1183–1186 (2002).
2. B. Alberts, The cell as a collection of protein machines: Preparing the next generation of molecular biologists. *Cell* **92**, 291–294 (1998).
3. N. N. Batada, L. D. Hurst, Evolution of chromosome organization driven by selection for reduced gene expression noise. *Nat. Genet.* **39**, 945–949 (2007).
4. T. Stoeger, N. Battich, L. Pelkmans, Passive noise filtering by cellular compartmentalization. *Cell* **164**, 1151–1161 (2016).
5. S. F. Banani, H. O. Lee, A. A. Hyman, M. K. Rosen, Biomolecular condensates: Organizers of cellular biochemistry. *Nat. Rev. Mol. Cell Biol.* **18**, 285–298 (2017).
6. A. A. Hyman, C. A. Weber, F. Jülicher, Liquid-liquid phase separation in biology. *Annu. Rev. Cell Dev. Biol.* **30**, 39–58 (2014).
7. C. P. Brangwynne *et al*., Germline P granules are liquid droplets that localize by controlled dissolution/condensation. *Science* **324**, 1729–1732 (2009).
8. A. W. Fritsch *et al*., Local thermodynamics govern formation and dissolution of *Caenorhabditis elegans P* granule condensates. *Proc. Natl. Acad. Sci. U.S.A.* **118**, e2102772118 (2021).
9. A. Molliex *et al*., Phase separation by low complexity domains promotes stress granule assembly and drives pathological fibrillization. *Cell* **163**, 123–133 (2015).
10. A. R. Strom *et al*., Phase separation drives heterochromatin domain formation. *Nature* **547**, 241–245 (2017).
11. Y. Shin, C. P. Brangwynne, Liquid phase condensation in cell physiology and disease. *Science* **357**, eaaf4382 (2017).
12. M. T. Wei *et al*., Nucleated transcriptional condensates amplify gene expression. *Nat. Cell Biol.* **22**, 1187–1196 (2020).
13. D. Deviri, S. A. Safran, Physical theory of biological noise buffering by multicomponent phase separation. *Proc. Natl. Acad. Sci. U.S.A.* **118**, e2100099118 (2021).
14. C. Zechner, F. Jülicher, Concentration buffering and noise reduction in non-equilibrium phase-separating systems. *Cell Syst.* **16**, 101168 (2025).
15. A. Klosin *et al*., Phase separation provides a mechanism to reduce noise in cells. *Science* **367**, 464–468 (2020).
16. C. A. Weber, C. Zechner, Drops in cells. *Phys. Today* **74**, 38–43 (2021).
17. M. Shamir, Y. Bar-On, R. Phillips, R. Milo, Snapshot: Timescales in cell biology. *Cell* **164**, 1302–1302 (2016).
18. M. Du *et al*., Direct observation of a condensate effect on super-enhancer controlled gene bursting. *Cell* **187**, 331–344 (2024).
19. A. K. Rai, J. X. Chen, M. Selbach, L. Pelkmans, Kinase-controlled phase transition of membraneless organelles in mitosis. *Nature* **559**, 211–216 (2018).
20. O. Mayr, The origins of feedback control. *Sci. Am.* **223**, 110–119 (1970).
21. J. C. Doyle, B. A. Francis, A. R. Tannenbaum, *Feedback Control Theory* (Courier Corporation, 2013).
22. K. Åström, T. Hägglund, *PID Controllers: Theory, Design, and Tuning* (ISA - The Instrumentation, Systems and Automation Society, 1995).
23. J. M. Edmunds, Control system design and analysis using closed-loop Nyquist and bode arrays. *Int. J. Control.* **30**, 773–802 (1979).
24. T. M. Yi, Y. Huang, M. I. Simon, J. Doyle, Robust perfect adaptation in bacterial chemotaxis through integral feedback control. *Proc. Natl. Acad. Sci. U.S.A.* **97**, 4649–4653 (2000).
25. H. El-Samad, J. Goff, M. Khammash, Calcium homeostasis and parturient hypocalcemia: An integral feedback perspective. *J. Theor. Biol.* **214**, 17–29 (2002).
26. T. Schmickl, I. Karsai, Integral feedback control is at the core of task allocation and resilience of insect societies. *Proc. Natl. Acad. Sci. U.S.A.* **115**, 13180–13185 (2018).
27. J. Behre, T. Wilhelm, A. von Kamp, E. Ruppin, S. Schuster, Structural robustness of metabolic networks with respect to multiple knockouts. *J. Theor. Biol.* **252**, 433–441 (2008).
28. E. Lee, A. Salic, R. Krüger, R. Heinrich, M. W. Kirschner, The roles of APC and AXIN derived from experimental and theoretical analysis of the WNT pathway. *PLoS Biol.* **1**, e10 (2003).
29. C. Y. Huang, J. E. Ferrell Jr., Ultrasensitivity in the mitogen-activated protein kinase cascade. *Proc. Natl. Acad. Sci. U.S.A.* **93**, 10078–10083 (1996).
30. H. Bode, *Network Analysis and Feedback Amplifier Design* (Bell Telephone Laboratories Series, D. Van Nostrand Company, Incorporated, 1945).
31. K. J. Åström, R. Murray, *Feedback Systems: An Introduction for Scientists and Engineers* (Princeton University Press, 2021).
32. N. Barkai, S. Leibler, Robustness in simple biochemical networks. *Nature* **387**, 913–917 (1997).
33. K. Åström, T. Hägglund, *PID Controllers: Theory, Design and Tuning* (Instrument Society of America, Research Triangle Park, ed. 2, 1995).
34. K. J. Åström, Model uncertainty and robust control. *Lect. Notes Iterative Identif. Control. Des.* **2000**, 63–100 (2000).
35. A. Gupta, M. Khammash, Frequency spectra and the color of cellular noise. *Nat. Commun.* **13**, 4305 (2022).
36. B. P. Ingalls, A frequency domain approach to sensitivity analysis of biochemical networks. *J. Phys. Chem. B* **108**, 1143–1152 (2004).
37. M. E. Csete, J. C. Doyle, Reverse engineering of biological complexity. *Science* **295**, 1664–1669 (2002).
38. J. Bauermann, S. Laha, P. M. McCall, F. Jülicher, C. A. Weber, Chemical kinetics and mass action in coexisting phases. *J. Am. Chem. Soc.* **144**, 19294–19304 (2022).
39. Y. Zhang *et al*., The exchange dynamics of biomolecular condensates. *eLife* **12**, RP91680 (2024).
40. L. Hubatsch *et al*., Transport kinetics across interfaces between coexisting liquid phases. *elife* **14**, RP10684 (2025).
41. T. Hirose, K. Ninomiya, S. Nakagawa, T. Yamazaki, A guide to membraneless organelles and their various roles in gene regulation. *Nat. Rev. Mol. Cell Biol.* **24**, 288–304 (2023).
42. L. de Monchaux-Irons, N. Han, B. Frühbauer, Volume buffering in multi-component phase separation. Research Square [Preprint] (2025). https://doi.org/10.21203/rs.3.rs-5433278/v1 (Accessed 23 April 2025).
43. M. Uchida *et al*., Quantitative analysis of yeast internal architecture using soft x-ray tomography. *Yeast* **28**, 227–236 (2011).
44. D. L. Lafontaine, J. A. Riback, R. Bascetin, C. P. Brangwynne, The nucleolus as a multiphase liquid condensate. *Nat. Rev. Mol. Cell Biol.* **22**, 165–182 (2021).
45. S. Laha, J. Bauermann, F. Jülicher, T. C. Michaels, C. A. Weber, Chemical reactions regulated by phase-separated condensates. *Phys. Rev. Res.* **6**, 043092 (2024).
46. P. J. Flory, Thermodynamics of high polymer solutions. *J. Chem. Phys.* **10**, 51–61 (1942).
47. M. L. Huggins, Some properties of solutions of long-chain compounds. *J. Phys. Chem.* **46**, 151–158 (1942).
48. C. A. Weber, D. Zwicker, F. Jülicher, C. F. Lee, Physics of active emulsions. *Rep. Prog. Phys.* **82**, 064601 (2019).
49. J. T. Overbeek, M. J. Voorn, Phase separation in polyelectrolyte solutions. Theory of complex coacervation. *J. Cell. Comp. Physiol.* **49**, 7–26 (1957).
50. G. L. Celora, R. Blossey, A. Münch, B. Wagner, Counterion-controlled phase equilibria in a charge-regulated polymer solution. *J. Chem. Phys.* **159**, 184902 (2023).
51. C. Wang *et al*., Stress induces dynamic, cytotoxicity-antagonizing TDP-43 nuclear bodies via paraspeckle LncRNA NEAT1-mediated liquid-liquid phase separation. *Mol. Cell* **79**, 443–458 (2020).
52. M. Novakovic *et al*., LLPS REDIFINE allows the biophysical characterization of multicomponent condensates without tags or labels. *Nat. Commun.* **16**, 4628 (2025).
53. N. O. Taylor, M. T. Wei, H. A. Stone, C. P. Brangwynne, Quantifying dynamics in phase-separated condensates using fluorescence recovery after photobleaching. *Biophys. J.* **117**, 1285–1300 (2019).
54. S. N. Rhoads, Z. T. Monahan, D. S. Yee, F. P. Shewmaker, The role of post-translational modifications on prion-like aggregation and liquid-phase separation of FUS. *Int. J. Mol. Sci.* **19**, 886 (2018).
55. K. M. Ruff, F. Dar, R. V. Pappu, Ligand effects on phase separation of multivalent macromolecules. *Proc. Natl. Acad. Sci. U.S.A.* **118**, e2017184118 (2021).
56. R. A. Hess, Simplified approach for modelling pilot pursuit control behaviour in multi-loop flight control tasks. *Proc. Inst. Mech. Eng. Part G J. Aerosp. Eng.* **220**, 85–102 (2006).
57. J. Jang, J. Yoo, Equivalent circuit evaluation method of lithium polymer battery using bode plot and numerical analysis. *IEEE Trans. Energy Convers.* **26**, 290–298 (2011).
58. Y. Xu *et al*., Electrochemical characteristics of cobaltosic oxide in organic electrolyte according to bode plots: Double-layer capacitance and pseudocapacitance. *ChemElectroChem* **6**, 2456–2463 (2019).
59. R. J. Smith *et al*., Stimulating native seizures with neural resonance: A new approach to localize the seizure onset zone. *Brain* **145**, 3886–3900 (2022).
60. W. Van Drongelen, Modeling neural activity. *Int. Sch. Res. Not.* **2013**, 871472 (2013).
61. J. T. Mettetal, D. Muzzey, C. Gómez-Uribe, A. van Oudenaarden, The frequency dependence of osmo-adaptation in saccharomyces cerevisiae. *Science* **319**, 482–484 (2008).
62. J. Dolan, J. Anderson, A. Papachristodoulou, "A loop shaping approach for designing biological circuits" in *2012 IEEE 51st IEEE Conference on Decision and Control (CDC)* (IEEE, 2012), pp. 3614–3619.
63. J. J. Teo, R. Weiss, R. Sarpeshkar, An artificial tissue homeostasis circuit designed via analog circuit techniques. *IEEE Trans. Biomed. Circuits Syst.* **13**, 540–553 (2019).
64. J. R. Buchan, mRNP granules: Assembly, function, and connections with disease. *RNA Biol.* **11**, 1019–1030 (2014).
65. P. Yang *et al*., G3bp1 is a tunable switch that triggers phase separation to assemble stress granules. *Cell* **181**, 325–345 (2020).
66. J. E. Henninger *et al*., RNA-mediated feedback control of transcriptional condensates. *Cell* **184**, 207–225 (2021).
67. B. S. Schuster *et al*., Controllable protein phase separation and modular recruitment to form responsive membraneless organelles. *Nat. Commun.* **9**, 2985 (2018).
68. N. A. Erkamp, R. Qi, T. J. Welsh, T. P. J. Knowles, Microfluidics for multiscale studies of biomolecular condensates. *Lab Chip* **23**, 9–24 (2023).